J Solid State Electrochem (2015) 19:769–783
DOI 10.1007/s10008-014-2668-8

ORIGINAL PAPER

Electrochemical behaviour of hybrid devices based on Na_2SO_4 and Rb_2SO_4 neutral aqueous electrolytes and carbon electrodes within wide cell potential region

Alar Jänes · Jaanus Eskusson · Leonard Mattisen · Enn Lust

Received: 18 December 2013 / Revised: 22 October 2014 / Accepted: 22 October 2014 / Published online: 19 November 2014

Abstract Focused ion beam scanning electron microscopy (FIB-SEM), X-ray photoelectron spectroscopy (XPS) and Brunauer–Emmett–Teller gas adsorption methods have been used for the characterisation of physical properties of microporous carbide-derived carbon electrodes, prepared from Mo_2C at 600 °C (noted as Mo_2C-CDC) before and after electrochemical tests conducted within a very wide two-electrode cell potential region. Cyclic voltammetry, constant current charge/discharge and impedance data have been analysed to establish the electrochemical characteristics of the hybrid devices consisting of the 1 M Na_2SO_4 and 1 M Rb_2SO_4 aqueous electrolytes and Mo_2C-CDC electrodes within the very wide cell potential region ($\Delta E \leq 2.4$ V). The influence of cation chemical composition on the electrochemical characteristics of supercapacitors/electrochemical hybrid devices has been analysed. The complex kinetics behaviour of completed devices (adsorption, blocking adsorption and intercalation of Na^+ and Rb^+ ions; faradic and mass transfer; gas adsorption; etc.) has been established at $\Delta E \geq 1.5$ V. At least three different characteristic time constants dependent on the electrolyte cation composition and cell potential applied have been established.

Keywords Carbide-derived carbon · Aqueous electrolyte · Supercapacitor · Hybrid electrochemical device

A. Jänes · J. Eskusson · E. Lust (✉)
Institute of Chemistry, University of Tartu, 14a Ravila Str., 50411 Tartu, Estonia
e-mail: enn.lust@ut.ee

L. Mattisen
Institute of Physics, University of Tartu, 14c Ravila Str., 50411 Tartu, Estonia

Introduction

Nowadays, mainly four types of electrochemical energy storage/conversion devices are under development: supercapacitors (SCs), batteries, electrolysers (ELs) and fuel cells (FCs) [1–6]. Batteries have higher specific energy than supercapacitors but lower specific power, and a very limited number of charging/discharging cycles can be applied [1–12]. Fuel cells and electrolysers [13–15] are characterised with high energy but moderate power density, and differently from supercapacitors, they are working in the stationary regime. Regardless of low energy density, the high power density supercapacitors are important energy storage systems, which can be used in various areas of modern technology, starting from the pulse energy generation/accumulation systems and finishing with the consumer goods [16–21]. For the high specific energy–specific power density application, the microporous carbon material [22, 23] and electrolyte characteristics have to be optimised [1–6, 8–11, 19–22]. Based on the results obtained [8–11, 19–23], the electrolyte chemical composition has a big influence on the electrochemical behaviour of aqueous and non-aqueous SCs [7–12, 23–26]. The potential advantages of H_2O-based supercapacitors would be the very cheap electrolyte applicable for SCs, regardless of the narrower region of ideal polarisability compared with that for non-aqueous SCs [8–11, 19–27]. For neutral Na_2SO_4 solution in H_2O and microporous and mesoporous carbons, the cell potential operation region from 1.0 up to 1.6 V [23–25], and even 1.9 V, has been demonstrated [26]. Of course, at $\Delta E \geq 1.6$ V, these systems are non-ideally polarisable and more detailed electrochemical analysis including impedance is inevitable, being the main aim of this paper.

Historically, SCs have been divided into two main groups: electrical double-layer capacitors and so-called hybrid supercapacitors [1–4, 8–11, 16–18]. However, based on our

earlier studies [8–11, 19–21], there is no rigid border between these types of SCs as some faradic reactions, including gas evolution (H_2 or surface oxidation and O_2 formation and evolution), can be observed outside of the low current density cell potential region (so-called electrical double-layer charging/discharging region, known as the region of ideal polarisability ΔE_{ideal}) observed for carbon | H_2O+xM Na_2SO_4 neutral electrolyte systems usually at $\Delta E \geq 1.4$ V. Thus, if the cell potential $\Delta E > \Delta E_{ideal}$, the nearly exponential increase of current density with cell potential is usually observed, where the faradic reduction reactions (reduction of H_3O^+ to H_2 and adsorption or intercalation of Li^+, Na^+, etc., cations as neutral atoms) at a negatively charged surface are main processes. H_2O decomposition or surface oxidation in a neutral medium at a positively charged surface is limited by the activation energy, strongly dependent on the pH of the solution, as well as on the electrode material used. For graphite electrodes, the H_2 evolution overvoltages η_{H2} as well as the surface oxidation/O_2 evolution overpotentials η_{ox} are usually very high [1, 8, 23].

Using the electrochemical kinetics data for metal electrodes [28], it was demonstrated that H_2 evolution overpotential η depends strongly on the cation adsorption energy, being highest for Cs^+-containing electrolytes (η_{H2} ~40 mV, compared with H^+ cations containing salts) due to the shift of ψ_1 potential toward more positive values (ψ_1 potential is the so-called Frumkin or double-layer correction potential, usually fixed/assumed for the plane (position in the Helmholtz layer)), where the electrochemical reaction takes place [28–32]. Thus, usually, it is assumed that the Frumkin correction depends on the chemical composition of the surface active cation used. However, for microporous–mesoporous electrodes, there are some objective complications connected with the establishment of the outer Helmholtz plane position due to the surface roughness and microporosity–mesoporosity, as well as macroscopic nonhomogeneity of the electrode surface [31–36].

This paper reports the results of the systematic studies of the electrochemical devices based on mainly microporous with a small amount of mesopores carbide-derived carbon (CDC) electrodes, prepared from Mo_2C (−325 mesh powder, Sigma-Aldrich) at T_{synt}= 600 °C, noted as Mo_2C-CDC, and 1 M Rb_2SO_4 or 1 M Na_2SO_4 aqueous electrolyte within the very wide two-electrode cell potential ΔE. The very high ΔE values have been applied to activate the faradic reactions at Mo_2C-CDC electrodes followed by the adsorption/absorption of formed H_2 and O_2 inside of the microporous Mo_2C-CDC electrode, as well as carbon electrode surface oxidation at very positive electrode potentials, increasing the faradic capacitance component.

Experimental

The SC electrodes were prepared from Mo_2C-CDC powder and from the mixture of binder (polytetrafluoroethylene, PTFE, 60 % solution in H_2O). The mixture received was laminated and roll pressed (HS-160N, Hohsen Corporation) to form a flexible layer of an active electrode material with thickness L=100±5 μm.

The crystallinity and macroscopic structure of the Mo_2C-CDC electrodes were evaluated by focused ion beam scanning electron microscopy (FIB-SEM)–energy-dispersive X-ray spectroscopy (EDX) and X-ray diffraction (XRD) (with a Cu anode to generate CuKα radiation (λ=1.5406 Å)). XRD data were collected in the 2θ range from 15° to 70° with the step size of 0.05°.

The FIB-SEM data have been obtained using Helios™ NanoLab 600. The X-ray photoelectron spectroscopy (XPS) experiments were carried out with a SCIEHTA SES-100 spectrometer by using an unmonochromated MgKα X-ray source with power of 300 W. The SES-100 system was calibrated using Au 4f photolines. The pressure in the analysis XPS chamber was within the range from 2×10^{-10} to 5×10^{-10} mbar.

The two-electrode standard stainless steel test cell (HS Test Cell, Hohsen Corporation) with two identical electrodes (flat cross-sectional area of one electrode ~2.0 cm^2) was completed with a manometer (Migishita Seiki Co.) for analysis of pressure inside of the cell. All electrochemical experiments were carried out at fixed temperature T=20±5 °C. A 25-μm-thick Celgard® 2400 separator sheet was used for mechanical separation of the working Mo_2C-CDC electrodes from each other. One molar Rb_2SO_4 and Na_2SO_4 aqueous electrolytes were used.

Results and discussion

Adsorption measurement data

Nitrogen adsorption measurements at liquid nitrogen temperature have been conducted using the Micromeritics ASAP 2020 surface area and porosity analysis measurement system. Based on the N_2 adsorption data for Mo_2C-CDC at T_{synt}= 600 °C, the multipoint Brunauer–Emmett–Teller (BET) surface area S_{BET}=1855 m^2 g^{-1}, micropore area (obtained using the *t-plot* method) S_{micro}=1823 m^2 g^{-1}, total pore volume V_{tot}=1.139 cm^3 g^{-1} and micropore volume V_{micro}= 1.077 cm^3 g^{-1} were calculated. The pore size distribution function vs. pore width plots, obtained using non-local density functional theory, shows two main peaks at d_1= 1.04 nm and d_2=2.64 nm, respectively. Thus, in addition to the micropores (d_1 lower than 2 nm according to IUPAC classification), there are some amount of mesopores (2 nm<d_2<50 nm, IUPAC) at/

inside of the Mo_2C-CDC, synthesised at T=600 °C. More detailed gas adsorption analysis has been given in our previous paper [18]. Thus, based on the N_2 sorption data and our previous SC studies [16–18], Mo_2C-CDC with hierarchical structure is an interesting material containing micropores for adsorption of charged ions and adsorption/absorption of gaseous H_2 or O_2 into micropores and mesopores. It should be mentioned that mesopores are needed for the quick mass transfer of reactants (H_3O^+ ions (or H_2O molecules)) into the micropores [22] as well for desorption of gaseous H_2 and O_2 from micropores into the neutral electrolyte solution.

FIB-SEM–EDX, Raman and XPS measurements

Focused ion beam scanning electron microscopy combined with the EDX (FIB-SEM–EDX) analysis method was used for the quantitative analysis of SC electrodes (Fig. 1a–d, Table 1). Similarly to the high-resolution transmission electron microscopy (HRTEM) data, discussed in [18], it was shown that the small amount of graphite-like carbon layers at the top (core level) of mainly amorphous carbon particles was observed. The Raman spectra were recorded using a Renishaw micro-Raman spectrometer equipped with a ×50 objective and 488 nm Ar^+ ion laser with maximum radiation power of 15 mW on the sample. XRD and Raman data, in agreement with HRTEM data, show that Mo_2C-CDC carbon has mainly an amorphous structure and only very slightly graphitized regions were found at the surface of some particles of Mo_2C-CDC material [11]. It was found that before electrochemical tests, the porous Mo_2C-CDC structure consists of particles with variable linear dimensions (from 10 to 100 nm). PTFE wires and lumps were observed between CDC particles, connecting the carbon particles into the flexible electrode layer (not shown for shortness). After electrochemical analysis (after 10, 100, 1000 and 10,000 charge/discharge cycles), the SC cells were opened and electrodes were washed many times

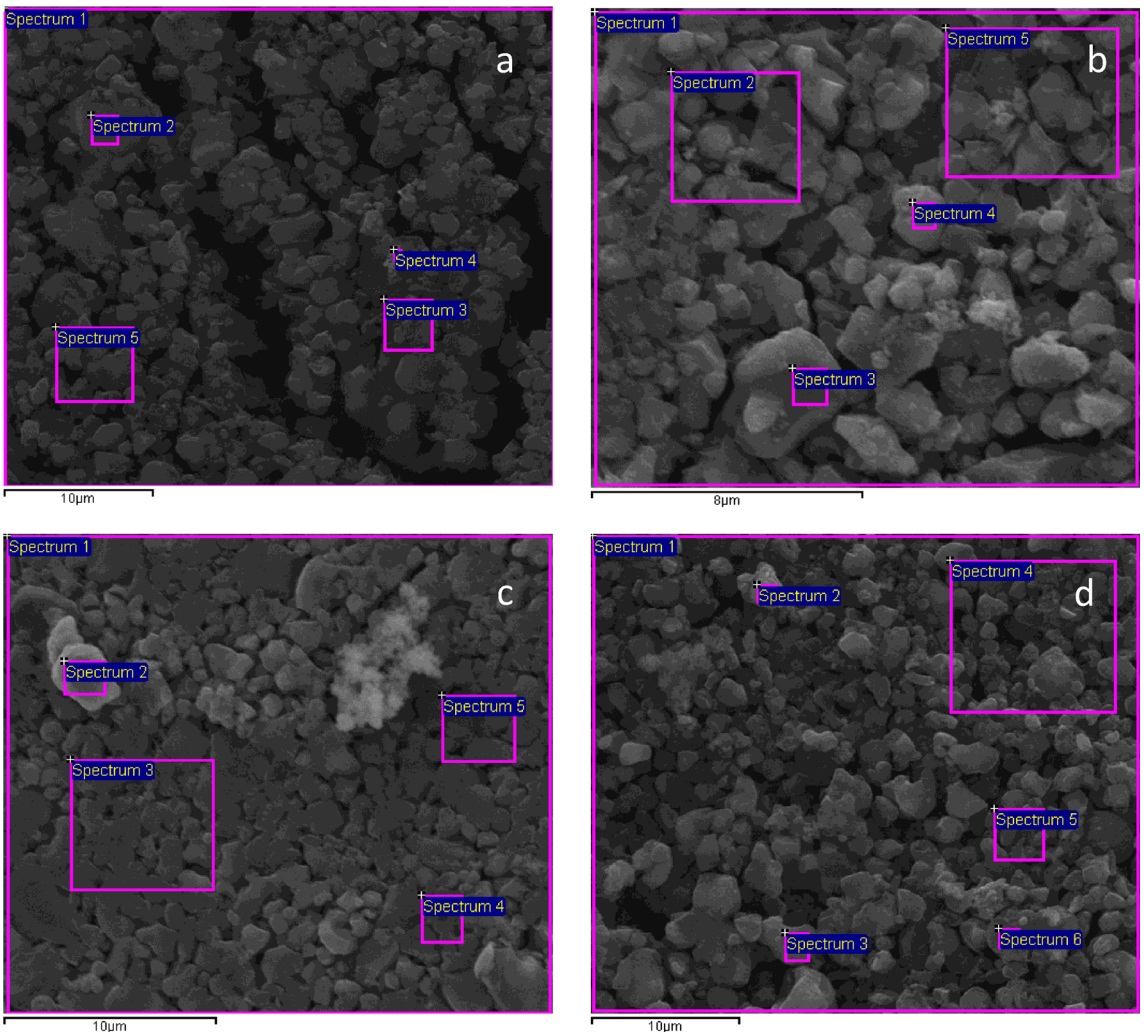

Fig. 1 Results of FIB-SEM analysis for Mo_2C-CDC electrodes in 1 M Rb_2SO_4 (**a**), 1 M Na_2SO_4 (**b**–**d**) and aqueous solutions for negatively (**a**–**c**) and positively (**d**) charged supercapacitor electrodes. Image **b** is taken from the membrane side and **c** from the current collector side Mo_2C-CDC electrode, tested in Na_2SO_4+H_2O solution, respectively

with clean Milli-Q$^+$ H_2O, dried under vacuum and analysed again using the FIB-SEM and XPS methods. It was demonstrated that in agreement with HRTEM data [18], there is no Cl^- or Cl_2 and/or other contaminants in electrode materials under testing.

A lot of signals connected with Rb (Fig. 1a, Table 1a) and Na (Fig. 1b, c, Table 1b, c) absorbed/deposited/intercalated into the negatively charged Mo_2C-CDC were found after 10,000 galvanostatic cycles in Rb_2SO_4 or Na_2SO_4 aqueous electrolyte, differently from the carbon electrodes measured after ten cycles (not shown for shortness) have been observed. Somewhat lower concentrations of Na^+ and Rb^+ have been observed in CDC after 1000 charge/discharge cycles (not shown for shortness). It should be noted that for positively charged Mo_2C-CDC, the concentration of Na was very low (Fig. 1d, Table 1d) indicating that the electrochemically activated accumulation of Na^+ ions (Na intercalation) has been taking place in the negatively charged electrode only.

Thus, during electrochemical potential cycling in the wide cell potential region, adsorption/absorption of Rb^+ and Na^+ ions and the intercalation (or chemisorption) of Rb and Na onto/into the Mo_2C-CDC electrode structure have been taking place. It should be mentioned that there is no big difference in amount of Rb or Na accumulated (data in Fig. 1a, b, Table 1a, b). It is surprising that a small amount of S (probably from SO_4^{2-} ions), especially from the Rb_2SO_4 solution, has been observed as well.

The XPS analysis data (Fig. 2) confirm the existence of adsorbed/intercalated Rb and Na (binding energy peak from 235 to 248 eV for Rb and at 498 eV for Na) onto/into the Mo_2C-CDC structure. Based on these results, the amount of the strongly covalently bonded Rb for Mo_2C-CDC electrodes observed after 10,000 galvanostatic cycles is remarkable. For electrodes studied after 100 cycles, the amount of covalently bonded Rb is smaller. For electrodes analysed after ten cycles, it was impossible to verify the existence of the Rb-C surface compound at all. It should be noted that the FIB-SEM–EDX and XPS are ex situ methods and, for more detailed studies, electrochemical in situ synchrotron radiation-based X-ray absorption spectroscopy [37] must be applied.

Cyclic voltammetry data

Cyclic voltammetry (CV) curves, expressed as capacitance for a symmetrical two-electrode system in 1 M Na_2SO_4, as well as in 1 M Rb_2SO_4 aqueous solutions, are given in panels a and b, respectively, of Fig. 3. The current density, j, measured at fixed cell potential scan rate v, has been used for calculation of the medium capacitance values according to Eq. 1:

$$C_{CV} = j\nu^{-1} \tag{1}$$

Equation 1 is correct if the capacitance C_{CV} is constant ($C_{CV} \neq f(E)$) [8, 19, 20] and/or the current density applied is small. In a symmetrical two-electrode system, the gravimetric capacitance $C_{m;CV}$ (F g^{-1}) for one activated carbon electrode can be obtained as follows:

$$C_{m;CV} = \frac{2C_{CV}}{m} \tag{2}$$

where m is the weight per one activated carbon electrode assuming that the positively and negatively charged electrodes have the same capacitance at fixed ΔE applied. The cyclic voltammetry curves expressed as capacitance vs. cell potential curves up to 1.3 V for 1 M Rb_2SO_4 and 1.2 V for Na_2SO_4, obtained at small voltage scan rates $v = d(E)//dt$, have nearly mirror image symmetry of the current responses about the zero current line (t is potential scanning time) characteristic of the ideal polarizability of the system under study. However, the discharging current densities, i.e. capacitance values for Rb_2SO_4 as well as for Na_2SO_4, depend on the final ΔE applied, indicating that the desorption of Rb^+ as well as Na^+ ions is slower than the adsorption step. At $1.3 \leq \Delta E \leq 1.5$ V, for both electrodes, a small increase in faradic current density has been observed, indicating that the hydrogen evolution and H_2O decomposition (or surface oxidation) at Mo_2C-CDC is a slow process due to the very high H_3O^+ electroreduction overvoltages [33–36].

However, for 1 M Rb_2SO_4 solution, the quick nearly exponential increase of j can be seen at $\Delta E \geq 1.3$ V. Surprisingly, there is nearly linear dependence of ΔE on log i (at $\Delta E \geq$ 1.3 V) (Fig. 4), known as the Tafel plot, if the individual electrode has been analysed. However, for the two-electrode system, ΔE vs. log i dependence characterises the behaviour of two different (or even more) electrode processes (or the behaviour of one electrode with the rate-limiting reaction kinetics). Therefore, the slope values of b and Tafel constant value a in the Tafel equation $\Delta E = a + b \log i$ calculated cannot be used for detailed and correct reaction mechanism analysis. The slope b value, characterising the complex electrochemical behaviour of the system, including the electroreduction step of hydrated protons ($H_3O^+ + e^- \rightarrow H_2O + H_{ads}$) and interaction of Rb through reaction ($Rb^+ + e^-$) and negatively charge electrode as well as the surface oxidation and O_2 evolution (H_2O oxidation) reaction at the positively charged Mo_2C-CDC | electrode interface, is very high for the Rb_2SO_4-based electrolyte.

For 1 M Na_2SO_4 solution, the intensive increase of current density starts already only at $\Delta E \geq 1.5$ V (Fig. 3). Differently

Table 1 Results of EDX analysis for Mo_2C-CDC electrodes in 1 M Rb_2SO_4 (a), 1 M Na_2SO_4 (b, c, d) and in aqueous solutions for negatively (a–c) and positively (d) charged supercapacitor electrodes

a

Spectrum	In stats.	C	O	F	S	Rb	Total
Spectrum 1	Yes	76.71	5.78	4.36	2.28	10.87	100
Spectrum 2	Yes	79.77	6.28	1.87	2.05	10.03	100
Spectrum 3	Yes	79.01	4.46	4.64	1.98	9.90	100
Spectrum 4	Yes	82.68	6.10	2.62	1.49	7.11	100
Spectrum 5	Yes	77.82	5.10	4.75	2.03	10.30	100
Mean		79.20	5.54	3.65	1.97	9.64	100
Std. dev.		2.27	0.76	1.32	0.29	1.46	
Max.		82.68	6.28	4.75	2.28	10.87	
Min.		76.71	4.46	1.87	1.49	7.11	

b

Spectrum	In stats.	C	O	F	Na	S	Total
Spectrum 1	Yes	41.04	44.36	7.08	6.63	0.89	100
Spectrum 2	Yes	42.36	44.29	5.95	6.30	1.10	100
Spectrum 3	Yes	48.21	42.45	3.46	5.23	0.64	100
Spectrum 4	Yes	39.50	36.33	16.70	6.44	1.03	100
Spectrum 5	Yes	42.74	42.57	6.86	6.69	1.14	100
Mean		42.77	42.00	8.01	6.26	0.96	100
Std. dev.		3.30	3.30	5.07	0.59	0.20	
Max.		48.21	44.36	16.70	6.69	1.14	
Min.		39.50	36.33	3.46	5.23	0.64	

c

Spectrum	In stats.	C	O	F	Na	S	Total
Spectrum 1	Yes	49.19	38.75	3.76	7.36	0.95	100
Spectrum 2	Yes	45.95	43.88	2.61	6.97	0.59	100
Spectrum 3	Yes	51.16	36.64	3.86	7.71	0.64	100
Spectrum 4	Yes	50.22	37.63	3.36	8.15	0.65	100
Spectrum 5	Yes	49.45	39.44	1.33	8.67	1.11	100
Mean		49.19	39.27	2.98	7.77	0.79	100
Std. dev.		1.97	2.79	1.05	0.66	0.23	
Max.		51.16	43.88	3.86	8.67	1.11	
Min.		45.95	36.64	1.33	6.97	0.59	

d

Spectrum	In stats.	C	N	O	F	Na	S	Total
Spectrum 1	Yes	81.58	2.60	9.52	5.16	0.30	0.85	100
Spectrum 2	Yes	83.75	2.94	9.56	2.94	0.18	0.63	100
Spectrum 3	Yes	83.57	2.52	9.51	3.14	0.37	0.89	100
Spectrum 4	Yes	83.38	2.52	8.49	4.36	0.44	0.81	100
Spectrum 5	Yes	83.36	1.90	6.20	7.35	0.44	0.75	100
Spectrum 6	Yes	85.44	2.48	6.89	4.17	0.37	0.64	100
Mean		83.51	2.49	8.36	4.52	0.35	0.76	100
Std. dev.		1.23	0.34	1.48	1.61	0.10	0.11	
Max.		85.44	2.94	9.56	7.35	0.44	0.89	
Min.		81.58	1.90	6.20	2.94	0.18	0.63	

Processing option: all elements analysed (normalised). All results in weight percent

from the Rb_2SO_4 electrolyte, there is no linear dependence of ΔE on log i (Fig. 4) within the $1.3<\Delta E\leq 1.5$ V region. Thus, only at $\Delta E\geq 1.5$ V the linear dependence of ΔE on log i has been observed with a noticeably lower slope value.

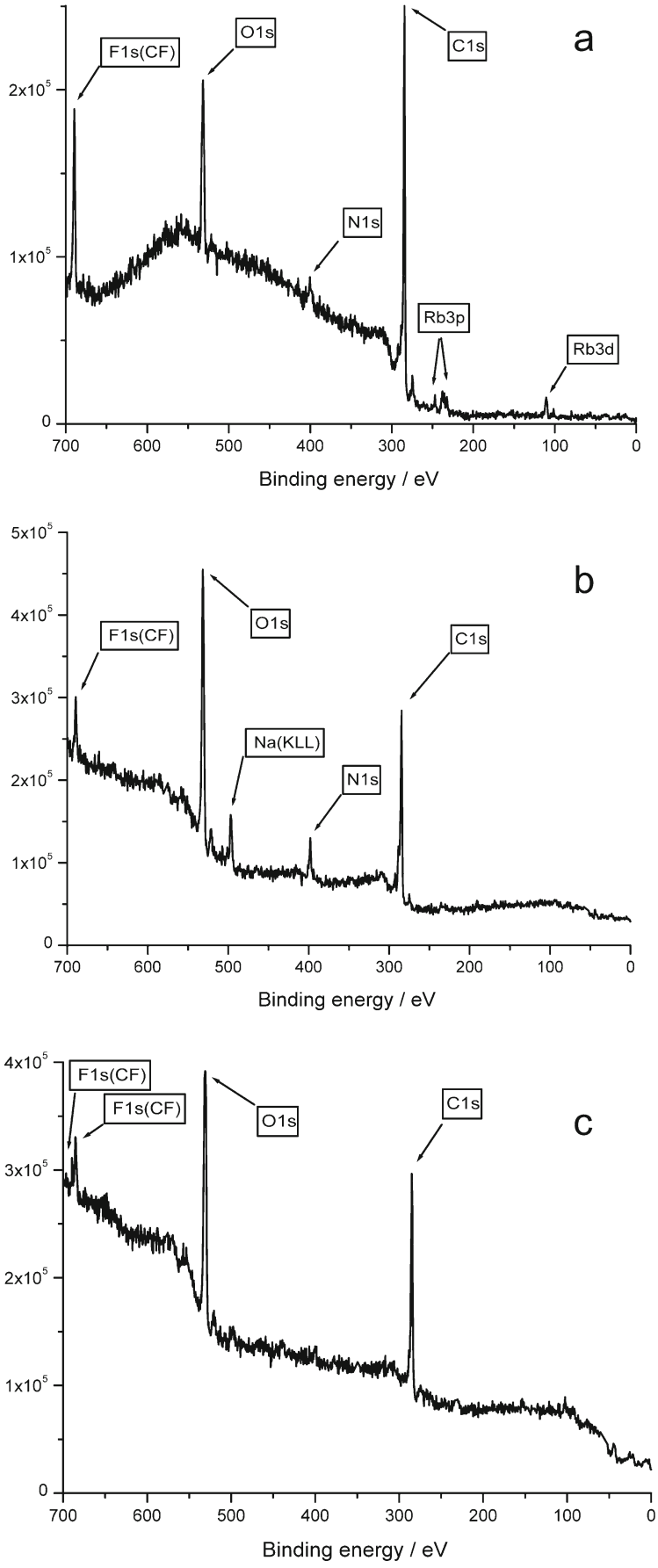

Fig. 2 XPS spectra for negatively (**a**, **b**) and positively (**c**) charged Mo_2C-CDC electrodes in 1 M Rb_2SO_4 (**a**) and 1 M Na_2SO_4 (**b**, **c**) aqueous solutions

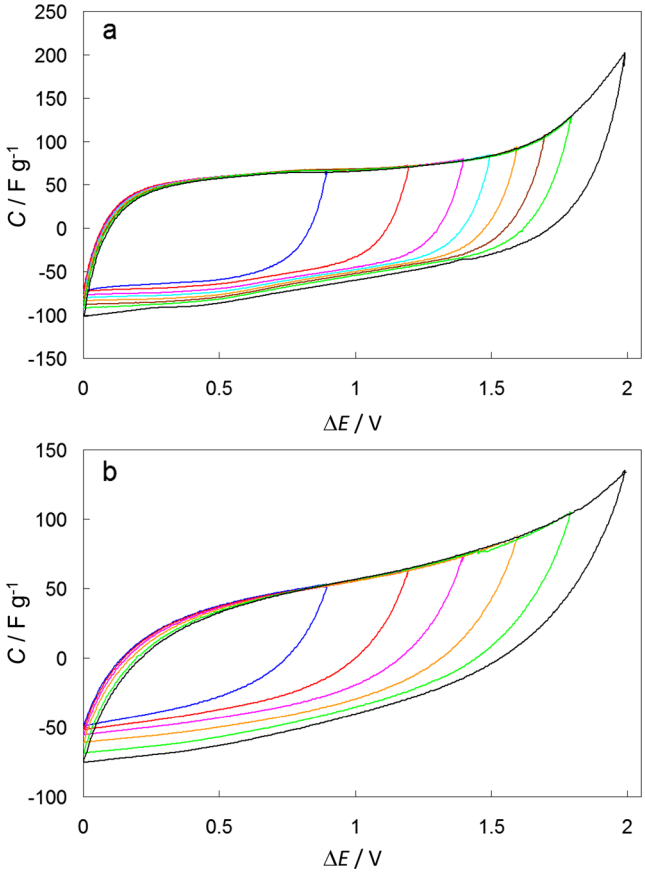

Fig. 3 Cyclic voltammetry curves expressed as capacitance C (per one electrode) vs. cell potential curves for supercapacitors in 1 M Na_2SO_4 (**a**) and in 1 M Rb_2SO_4 (**b**) at potential scan rate 10 mV s^{-1} at different maximal cell potentials

Considerably different slope values (Fig. 4) for these two systems indicate that in addition to H_2 evolution and surface oxidation, the adsorption and reduction (intercalation) of cations play a probably important role. The intensive increase of the faradic process(es), i.e. hydrogen and O_2 (surface oxidation) evolution, is shifted ~150±5 mV toward higher ΔE values for the Rb_2SO_4 solution, indicating that the hydrogen and oxygen evolution overvoltages at Mo_2C-CDC from 1 M Na_2SO_4 solution are somewhat lower than that for 1 M Rb_2SO_4. This is in very good agreement with H_2 evolution data established for Hg and other metal electrodes [28], indicating that the Na^+ or Rb^+ adsorption influences the ψ_1 potential similarly to high hydrogen overvoltages measured for metals (Hg, Pb, Bi, Cd). Thus, the adsorption of Rb^+ (similarly to Cs^+) cations increases the hydrogen as well as the oxygen evolution overvoltages [28, 33–36]. It is surprising that during the first very wide cell voltage cycles (ΔE=2.0 V), the charging (reduction/oxidation) curve is very well reproducible and only a weak increase of discharging currents (reoxidation of H_2 and reduction of oxygen containing surface functionalities) can be seen after 100 or 1000 cycles but especially after 10,000 cycles (not shown for shortness).

After the polarisation of electrodes at cell $\Delta E \geq 2.4$ V in the discharging curve at $\Delta E < 1.0$ V, only a very small and very wide current peak (plateau) (Fig. 5) has been observed, indicating the reoxidation of H_2 adsorbed/absorbed in porous Mo_2C-CDC, as well as the reduction of the oxygenated functional groups at the electrode surface. Faradic hydrogen reoxidation (ionisation) and surface reduction processes at the Mo_2C-CDC electrode surface, within the region of ΔE studied, are very slow and irreversible processes as there are no clearly visible current peaks in the discharging curve at lower cell potentials and wide potential scan rates, v, applied.

A comparison of current densities measured in 1 M Na_2SO_4 and 1 M Rb_2SO_4 solutions indicates that both electrodes can be applied within the very wide ΔE region; however, for the Rb_2SO_4-based electrolyte, the faradic current densities are clearly lower (Figs. 3 and 5) due to the blocking

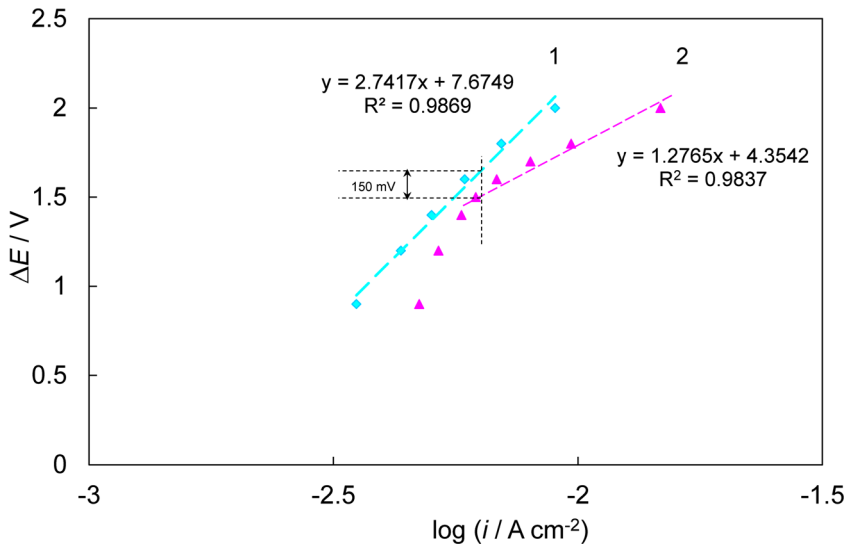

Fig. 4 ΔE vs. log i dependencies for hybrid electrochemical devices in 1 M Rb_2SO_4 (*1*) and in 1 M Na_2SO_4 (*2*) aqueous electrolyte

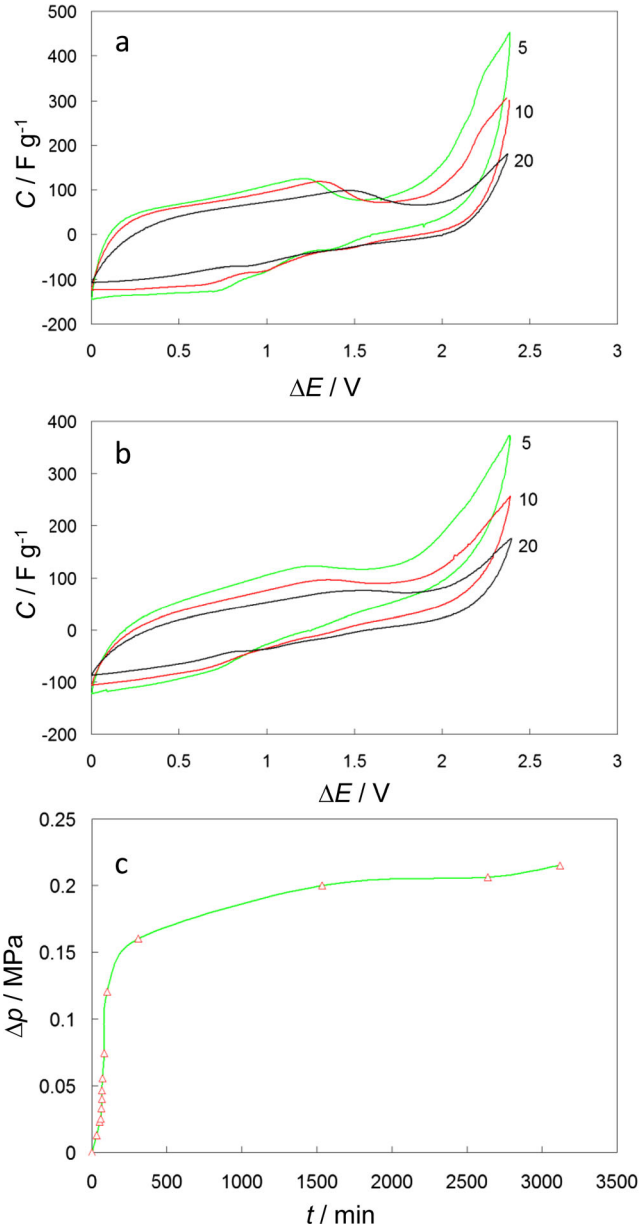

Fig. 5 Cyclic voltammetry curves expressed as capacitance C vs. cell potential curves in 1 M Na_2SO_4 (**a**) and in 1 M Rb_2SO_4 (**b**) at different cell potentials and at different potential scan rates, noted in the figure. Hybrid electrochemical device cell pressure vs. time dependence in 1 M Rb_2SO_4 (**c**) and at cell potential 2.4 V

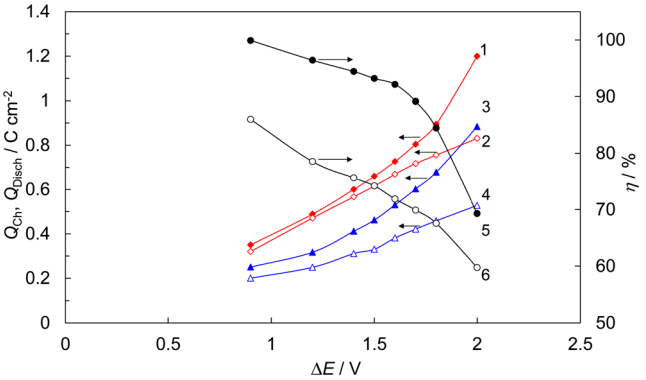

Fig. 6 Surface charge density (*1*–*4*) and coulombic efficiency η (*5*, *6*) vs. cell potential curves for the Mo_2C-CDC-based cell in 1 M Na_2SO_4 (*1*, *2*, *5*) and 1 M Rb_2SO_4 (*3*, *4*, *6*) for charging (*1*, *3*) and discharging (*2*, *4*), noted in the figure

adsorption of Rb^+ at the negatively charged Mo_2C-CDC electrode (Figs. 1 and 2).

The activation of microporous and mesoporous Mo_2C-CDC electrodes takes place only at $\Delta E \geq 1.5$ V. Thus, $C_{m;CV}$ increases with the decrease of the potential sweep rate applied, indicating a slow rate of reduction and oxidation reactions occurring at negatively and positively charged electrodes. Data in Fig. 5a, b show that the high capacitance values have been calculated in the high-current-density (hydrogen/oxygen evolution/surface oxidation) region, explained by the high faradic process capacitance values for hydrogen and oxygen evolution reactions.

At $v > 5$ mV s^{-1} and $\Delta E > 1.7$ V, the C values are lower for the Rb_2SO_4 electrolyte-based SC explained by the higher hydrogen overvoltage for 1 M Rb_2SO_4 solution than that for Na_2SO_4. Thus, the adsorption/reduction/intercalation of Rb^+ cations onto the Mo_2C-CDC surface causing the shift of the zero total charge potential (and the ψ_1 potential) toward the less negative electrode potential increases the hydrogen and oxygen evolution overpotential (~0.04 V).

For the verification of hydrogen and oxygen evolution processes, the pressure inside of the hermetic test cell was monitored. It is surprising that during the first 10–20 min, there was no big increase of pressure inside of the cell during the first cycles or even during short-time holding ($t < 3$ min) of the cell at $\Delta E = 2.4$ V (Fig. 5c). Only during long-lasting holding (1–1.5 h) of the two-electrode cell at 2.4 V the small overpressure in cells has been observed, as demonstrated in Fig. 5c. As can be seen in Fig. 5c, during 50 to 500 min polarisation at $\Delta E = 2.4$ V, the pressure inside of the cell increases nearly exponentially and, after polarisation during 1000–1500 min (at $\Delta E = 2.4$ V), the increase in Δp practically stopped. To the first very rough approximation, this surprising result can be explained by the adsorption/absorption of generated hydrogen/oxygen onto/into the porous Mo_2C-CDC electrode [28–30, 33–35].

Surface charge density potential curves (at potential scan rate 10 mV s^{-1}) have been integrated to obtain the surface charge density Q, ΔE curves (Fig. 6). A comparison on Q, ΔE curves for charging and discharging cycles indicates that the electrochemical coulombic efficiency η noticeably decreases with the increase of ΔE applied, if $\Delta E \geq 1.5$ V. A somewhat lower η has been calculated for the Rb_2SO_4-based system, explained by the blocking adsorption of Rb^+ cations into the negatively charged Mo_2C-CDC electrode. The cyclic voltammetry and coulombic efficiency data show that systems

under discussion can be used as combined electricity storage, i.e. H_2/O_2 generation/storage systems however with quite low efficiency at $\Delta E \geq 1.5$ V. However, it is very interesting to mention that even at $\Delta E = 1.8$ V, the electrochemical reversibility of the Mo_2C-CDC | 1 M Na_2SO_4 system is higher ($\eta \geq 85$ %) than that for lead accumulators ($\eta \leq 80$ %) [1]. A very quick decrease of η has been established for the Rb_2SO_4-based system at $\Delta E \geq 1.5$ V.

Constant current charge/discharge data

The SC cells were tested at constant current (CC) charge/discharge regimes (from 1 to 50 mA cm^{-2}) within the different voltage range from 0 to 1.2, from 0 to 1.5 and from 0 to 2.0 V (Fig. 7a), and from 1.0 to 2.0 V (Fig. 7b). CC curves obtained for the normal ΔE region (0–1.2 V) have a very nice traditional shape [23] characteristic of ideally polarisable systems (not shown for shortness). However, Fig. 7a, b shows that the very complicated charging/discharging curves have been measured if the wider ΔE region has been applied: 0 V$<\Delta E<$2.0 V or 1.0 V$<\Delta E<$2.0 V. In principle, the two nearly linear charging regions have been observed: first at lower cell potentials (0.5$<\Delta E<$1.0 V, double-layer charging) and second from 1.3 V$<\Delta E<$1.8 V (probably mainly H_3O^+ reduction and Na^+ or Rb^+ adsorption). In discharging CC curve, the linear regions have been observed at 1.2 V$<\Delta E<$ 1.9 V and 0.1 V$<\Delta E<$1.0 V. Interestingly, if these cells have been cycled within the limited cell potential region (1.0 V$<\Delta E<$2.0 V), the discharging curves are non-linear within the all potential region (1.0$<\Delta E<$2.0 V) applied, indicating that after the gas (H_2, O_2) formation/adsorption step at $\Delta E>$ 1.2 V, the gas desorption and ionisation is only possible at

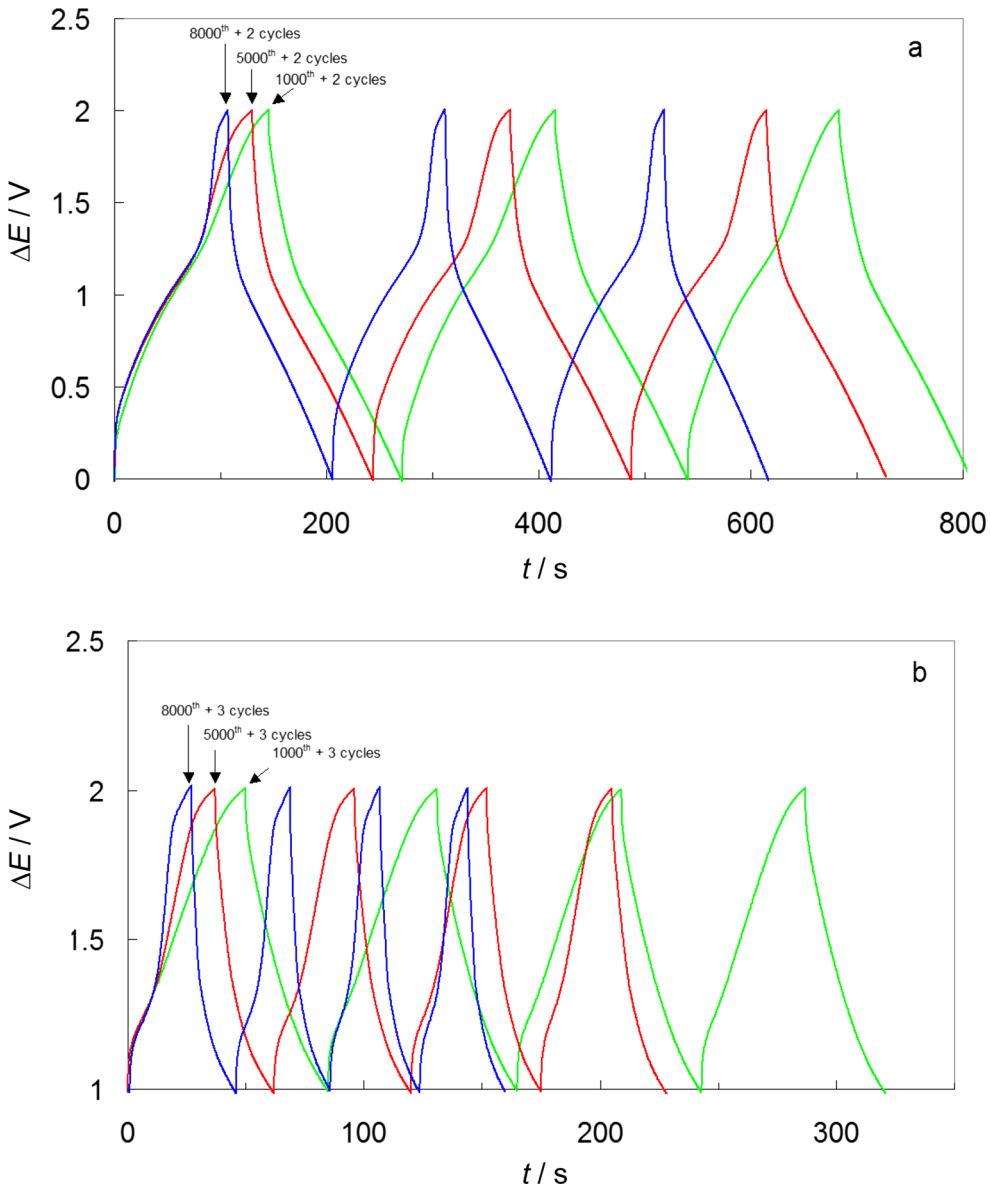

Fig. 7 Galvanostatic charging/discharging curves for the Mo_2C-CDC-based cell in 1 M Rb_2SO_4 at current density 5 mA cm^{-2} at cell potential from 0 to 2 V (**a**) and from 1 to 2 V (**b**)

lower cell potentials than $\Delta E<1.0$ V due to the very high activation energy of H_2 or O_2 ionisation step(s). Thus, the H_2 and/or O_2 ionisation and surface oxide reduction and cation desorption have very high overvoltages at Mo_2C-CDC electrodes.

Usually, the capacitance of the cell (C_{CC}) at $\Delta E\leq 1.2$ V will be obtained from the slope of the discharge curve according to Eq. 3:

$$C_{CC} = j\frac{dt}{d(E)} \quad (3)$$

where $dt/d(E)$ is the slope of the discharge or charging curve with corresponding current density j.

From the constant current charge/discharge curves, the value of internal resistance, R_{CC}, from the *IR*-drop is observable after the changing of the charging or discharging current direction has been calculated ($R_{CC}=dE_1/2j$, where dE_1 is the value of cell potential for 10 ms). The lowest R_{CC} value has been calculated for the 1 M Rb_2SO_4+H_2O-based cell compared with the Na_2SO_4+H_2O-based cell, explained by the higher molar conductivity of the Rb_2SO_4 aqueous solution in agreement with the analysis of impedance data (next chapter) and limiting ionic (molar) conductivity values λ (S cm^2 mol^{-1}: Na^+ 50.10, Rb^+ 77.8, SO_4^{2-} 160). At $\Delta E\leq$ 1.5 V, where the gas formation is slow and unimportant, the *IR*-drop is practically independent of the cycle number applied. However, the R_{CC} value slightly increases with the cell potential applied at $\Delta E\geq 1.5$ V, explained by the accumulation of H_2 and O_2 (or surface oxides) inside of the porous carbon matrix and squeezing out of some electrolytes from the microporous matrix, and/or by blocking adsorption/intercalation of Na or Rb atoms into the porous matrix, decreasing the linear dimensions of the pore.

For the Mo_2C-CDC | 1 M Na_2SO_4 or Mo_2C-CDC | 1 M Rb_2SO_4 aqueous interface, there is no remarkable dependence of the relative capacitance, $C_{rel}=C_{in}/C_x$, or relative resistance, $R_{rel}=R_{in}/R_x$, on the galvanostatic cycle number applied (C_{in} and C_x are the capacitance values of the third and x number cycle, respectively, and R_{in} and R_x are the corresponding series resistance values, calculated from the *IR*-drop), if $\Delta E<1.3$ V. Hence, for 1 M Na_2SO_4 and 1 M Rb_2SO_4 | Mo_2C-CDC interfaces, C_{rel} and R_{rel} are quite stable and these salts can be used as aqueous electrolytes for SCs at $\Delta E\leq 1.3$ V.

The coulombic cycling efficiency, i.e. the so-called round trip efficiency (RTE) has been calculated as a ratio of capacitances measured during discharging and charging of SCs, if $\Delta E\leq 1.3$ V. The highest RTE ≥98 % at $\Delta E<1.3$ V has been calculated for 1 M Rb_2SO_4 aqueous supercapacitors and RTE ≥96 % for 1 M Na_2SO_4, demonstrating the reasonable dependence of RTE on the electrolyte conductivity discussed before. This effect can be explained by the influence of the *IR*-drop as well as the mass transfer and partial charge transfer resistances on the total charge accumulation efficiency, because the solvation (standard molar hydration enthalpy ΔH) of Rb^+ ions in H_2O is somewhat lower than that for Na^+ ions (ΔH (kJ mol^{-1}) $Na^+=-321$ and $Rb^+=-300$, respectively). Thus, the adsorption/absorption kinetics of ions (reversibility of charging/discharging of the system) depends on the hydration of cations applied as an electrolyte for SC. Formation of H_2 and O_2 gases or surface compounds as adsorbed/intercalated reaction products or surface oxides onto/into some places of electrode material at higher ΔE is possible, but a weak influence on the RTE of supercapacitors based on the 1 M Na_2SO_4 or 1 M Rb_2SO_4 electrolyte indicates that this effect is quite unimportant at lower $\Delta E\leq 1.3$ V. In addition, the physical adsorption/intercalation of Rb^+ ions at/into the Mo_2C-CDC electrode shifts the zero charge potential toward more positive values (~30 mV), thus increasing the ψ_1 potential values at the outer Helmholtz plane and therefore increasing the H_2 evolution overpotential.

However, for systems tested at $\Delta E>1.3$ V, Eq. 3 cannot be applied as the charging/discharging curves are non-linear. Therefore, for the more detailed analysis, the charging/discharging curves have been integrated to obtain the charge densities accumulated during charging Q_{ch} and discharging Q_{disch} steps. The calculations show that in agreement with CV data, the coulombic efficiency is quite low ($\eta\leq 0.8$) at $\Delta E>$ 2.3 V. The very quick decrease of Q_{ch} and Q_{disch} takes place after application of a comparatively small number of charging/discharging cycles ($N_{cyc}>1000$ at $\Delta E>1.5$ V), explained by the quick electrode degradation process after/during gas evolution, adsorption/deionisation steps or by the adsorption/absorption/intercalation of Na^+ or Rb^+ ions (thus Na or Rb atoms) into the microporous Mo_2C-CDC electrodes.

Analysis of Nyquist and Bode plots

The Nyquist plots [19–21, 38–44], given in Fig. 8a, b for SCs completed from Mo_2C-CDC electrodes in 1 M Rb_2SO_4 or 1 M Na_2SO_4 aqueous solutions, have been measured within the wide range of ac frequency, f (from 1×10^{-3} to 1×10^5 Hz), and at fixed cell potentials from ΔE=1.2 to 2.0 V. At the very beginning of the experiments, if $\Delta E\leq 1.2$ V, the Nyquist plot has a traditional shape (not shown for shortness) [8–11, 19–21, 23] and they consist mainly of three parts: (1) the very small and noticeably depressed semicircle at higher ac frequency ($f\geq 3$ Hz) with a characteristic frequency, f_{max} (obtained as the frequency at the maximum in the Nyquist plot) (the semicircle shape depends on the adsorption kinetics of ions at the microporous electrode and on the series resistance of a material, mass transfer resistance inside the meso/macroporous carbon structure as well as on the mass transfer resistance in the micropores); (2) the so-called double-layer capacitance region ("knee" at low frequencies $f<$ 0.01 Hz), obtained by the finite-length adsorption effect; and

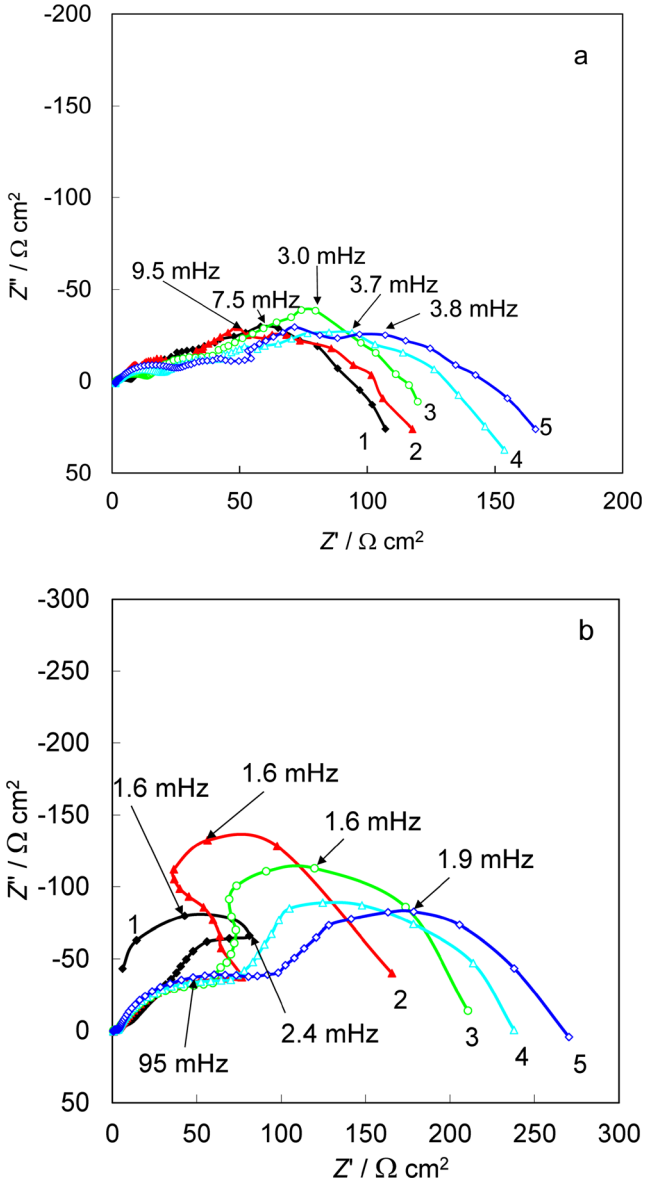

Fig. 8 Nyquist ($-Z''$, Z') plots for hybrid electrochemical devices at ΔE= 2.0 V in 1 M Na_2SO_4 (**a**) and 1 M Rb_2SO_4 (**b**) aqueous electrolyte after 1000 (*1*), 2000 (*2*), 3000 (*3*) 4000 (*4*) and 5000 (*5*) cycles at constant current charging/discharging cycles from 0 to 2.0 V

(3) the not very-well-expressed so-called "porous" region with a slope of $\alpha \approx 45°$, characteristic of the mass transfer-limited processes in the microporous–mesoporous matrix of an electrode.

At $\Delta E \geq 1.3$ V, the Nyquist plots for the Na_2SO_4-based SC have a very complicated shape and at least five different areas in Z'', Z' plots have been established (shown in Fig. 8a, b). With the increase of $\Delta E \geq 1.5$ V applied, the role of faradic processes rises quickly (formation of the semicircle in Nyquist plots at $f<10$ mHz). Differently from data measured at $\Delta E \leq$ 1.3 V, Nyquist plots at a lower region of ac $f<1$ Hz and at 2.0 V are non-linear and deviate strongly from a nearly vertical line explained by the deviation of the Na_2SO_4 | Mo_2C-CDC interface from the simple adsorption-limited step (ideal capacitive) behaviour.

According to the experimental data given in Fig. 8b, the Nyquist plots at ΔE=2.0 V for the Rb_2SO_4 solution have an even more complicated shape, compared with the Na_2SO_4-based SC, explained by the strong specific adsorption and intercalation of Rb^+ being possible at $\Delta E \geq 2.0$ V (Fig. 8b). The shape of the Nyquist plot depends on the number of cycle analysed more pronounced for the Rb_2SO_4-based system. The relaxation frequency for the kinetically mixed so-called very-low-frequency process ($f<4$ mHz) depends noticeably on the electrolyte studied, and f_{low} increases from 1.9 mHz (1 M Rb_2SO_4) to 3.8 mHz for 1 M Na_2SO_4. Thus, the characteristic relaxation time $\tau_{max}=(2\pi f_{max})^{-1}$ decreases from 0.1 s (1 M Rb_2SO_4) to 0.04 s (1 M Na_2SO_4), explained by the stronger chemical interaction of Rb^+ cations with the Mo_2C-CDC surface caused by the lower hydration energy values for Rb^+ ions compared with Na^+ ions [31, 32]. In addition, the stronger adsorption bond for Rb^+-containing systems is caused by the smaller hydration number for Rb^+ (~4) compared with that for Na^+ (~6) as well as explained by the shorter effective Debye length values (shorter distance of the closest approach of Rb^+ to the surface for weakly solvated Rb^+ ions compared with strongly hydrated Na^+ ions) [31, 32].

Thus, probably, dependency of the shape and the slope for the Nyquist plot in the low-frequency region on the SC cell voltage is mainly caused by the rate of the electrical double-layer formation and Rb^+ adsorption/intercalation processes inside of the mesoporous and microporous carbide-derived carbon electrodes. However, mainly the adsorption-limited step for 1 M Na_2SO_4 and 1 M Rb_2SO_4 electrolyte-based systems has been established only at $\Delta E \leq 1.3$ V (not shown for shortness). The dependence of the shape of the Nyquist plots on the cell voltage at $f<0.01$ Hz (so-called finite-length effect region) is mainly caused by the decrease of the effective screening length, well visible for the 1 M Rb_2SO_4 and 1 M Na_2SO_4 electrolytes with increasing cell potential. The effective diffuse layer thickness as a function of the electrode rational potential E_R is given as $\kappa_{eff}(E_R)=2/\kappa\cos(e\beta E_R)$, where $\kappa_{eff}(E_R)$ and κ are the effective and usual Gouy lengths and E_R is a potential with respect to the zero charge potential, $\beta=(R_BT)^{-1}$, where T is the absolute temperature and R_B is the Boltzmann constant [39, 40]. Thus, the dependence of the shape of the Nyquist plot within the very-low-frequency region on cell voltage, to a first approximation, indicates that the pore dimension is in the same order of magnitude as the effective Debye length for the 1 M electrolyte solutions, i.e. the pore dimension is comparable to the effective diameter of the partially desolvated Rb^+ or Na^+ ions absorbed [38–40]. A similar dependence of the screening length and effective diffuse layer thickness has been established for specifically adsorbed anions [38].

Preliminary non-linear least squares fitting data show that in addition to the slow adsorption and faradic charge transfer steps ($f \geq 100$ mHz) as well as the finite-length Warburg-like mass limited transfer steps (5 mHz$<f\leq$50 mHz), the inductive behaviour ($f<2.4$ mHz, Fig. 8b), initiated by the so-called corrosion of electrode material or irreversible blocking adsorption, surface oxide layer formation process, etc., are involved. In addition, accumulation of the gases (H_2 and O_2) into the microporous volume of Mo_2C-CDC at $\Delta E>1.5$ V and reionisation $\Delta E<1.0$ V occur in agreement with the rise of high-frequency series resistance of the system under discussion (Fig. 8a, b). It should be noted that the exact fitting of Nyquist plots at $\Delta E>1.5$ V and $f<100$ mHz was impossible due to very many processes involved.

The analysis of the Bode phase angle θ, log f plots and log ($-Z''$), log f plots (Fig. 9a–c) shows that differently from the Mo_2C-CDC | 1 M $(C_2H_5)_3CH_3NBF_4$+acetonitrile (non-aqueous) interface ($\Delta E\leq 3.0$ V) for aqueous Na_2SO_4 and Rb_2SO_4 solutions at $\Delta E<1.0$ V, at $\Delta E\geq 1.3$ V, there are noticeable deviations from the ideally polarisable interface model for Rb_2SO_4 and Na_2SO_4 solutions within all ac frequency region studied. For the Mo_2C-CDC | 1 M Na_2SO_4 or 1 M Rb_2SO_4+H_2O system, at least four different regions characterised by different time constants can be calculated. At $\Delta E=2.0$ V, the data in Figs. 8 and 9 show that the very-high-frequency region $f_{high}\geq 10$ kHz is noticeably shorter for the Rb_2SO_4-based system compared with Na_2SO_4. The high-frequency minimum (i.e. maximum with negative δ values) in δ, log f plot is shifted nearly one order toward lower f values for the Na_2SO_4-based system compared with that for Rb_2SO_4.

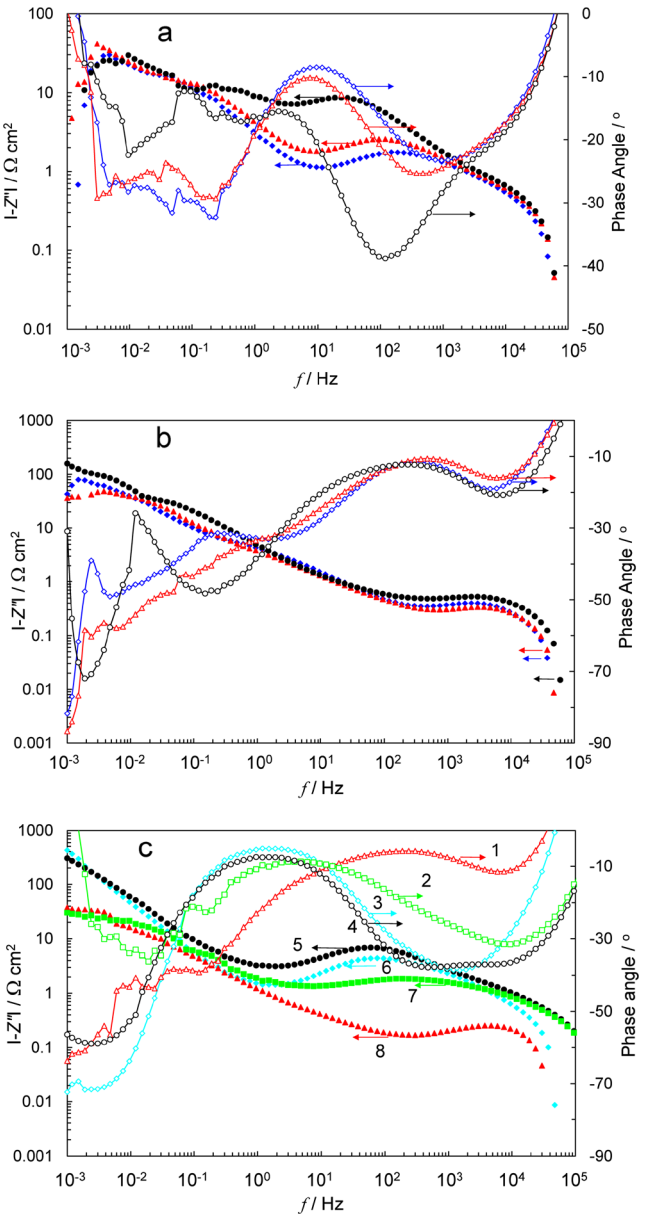

Fig. 9 Bode phase angle, log f and log ($-Z''$), log f plots for hybrid electrochemical devices in 1 M Na_2SO_4 (**a**) and in 1 M Rb_2SO_4 (**b**) at $\Delta E=2.0$ V in aqueous electrolyte after 1000 (*rhombs*), 2000 (*triangles*) and 5000 cycles (*circles*) at current charging/discharging test from 0 to 2.0 V. *Open symbols* correspond to the Bode phase angle (expressing the magnitude of the frequency response gain), and *filled symbols* correspond to the log ($-Z''$), log f plots. Corresponding Bode phase angle, log f plots (*1–4*) and log ($-Z''$), log f plots (*5–8*) in 1 M Na_2SO_4 (*1*, *3*, *6*, *8*) and in 1 M Rb_2SO_4 (*2*, *4*, *5*, *7*) at $\Delta E=2.0$ V (*1*, *2*, *7*, *8*) at $\Delta E=1.0$ V (*3*, *4*, *5*, *6*) (**c**), noted in the figure

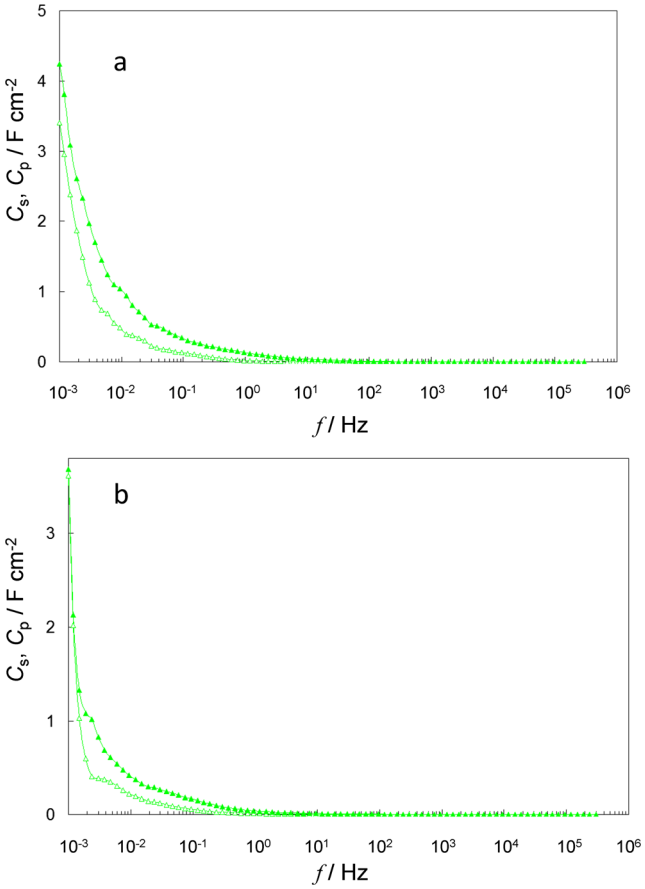

Fig. 10 Gravimetric series (C_s) (*filled triangles*) and parallel (C_p) (*open triangles*) capacitances vs. frequency plots at $\Delta E=2.0$ V for hybrid electrochemical devices in 1 M Na_2SO_4 (**a**) and in 1 M Rb_2SO_4 (**b**)

The $|\delta|$ values are higher ($|\delta|=40°$) for the Na_2SO_4-based system than for the Rb_2SO_4-based SC ($|\delta|=20°$), indicating the more pronounced mixed kinetics for Rb_2SO_4 and lower ratio adsorption but more pronounced mass transfer processes for the Na_2SO_4-based SC.

Phase angle absolute values are nearly comparable with the so-called medium-frequency ac (from 0.2 to 10 Hz for Na_2SO_4 and from 1.0 to 500 Hz or Rb_2SO_4) region, indicating that the faradic processes are mainly occurring at the Mo_2C-CDC electrode surfaces. Within the low-frequency ac region $f_{low}<1$ Hz for Rb_2SO_4 and $f_{low}<2$ Hz for Na_2SO_4, the second minimum in δ, log f plots can be seen indicating the slow mixed kinetics processes (faradic mass transfer and adsorption step-limited processes) at the Mo_2C-CDC | electrolyte interface. Within the very-low-frequency ac region, $f<2.4$ mHz, the phase angle values increase to zero, indicating that the very slow faradic reaction(s) determine(s) the Na_2SO_4 or Rb_2SO_4 aqueous solution | Mo_2C-CDC interface behaviour.

The relaxation frequency for the high-frequency process f_{high} from 100 to 500 Hz for the Na_2SO_4-based system depends noticeably on the cycle number applied. With the increase of cycle number applied from 1 to 1000, there is no big shift of f_{high} values, but f_{high} decreases very remarkably after 2000 or 5000 cycles ($f_{high}=120$ Hz). Surprisingly, $f_{high}=8000$ Hz is noticeably higher for the Rb_2SO_4-based SC and there is no remarkable shift of f_{high} with the cycle number (material degradation step) studied.

Interestingly, the low-frequency processes $f_{med}=0.3$ Hz have systematically lower values for the Na_2SO_4-based SC compared with $f_{med}=5$ Hz for the Rb_2SO_4-based supercapacitor. At very low frequency, there are no clearly visible maxima in phase angle absolute value, log f plots, and the $|\delta|$ are approaching zero, indicating that the very slow faradic processes are rate-determining processes for the Na_2SO_4- and Rb_2SO_4-based SC (Fig. 9a, b). At f_{med} and f_{high} frequency regions, the mixed kinetics processes take place at

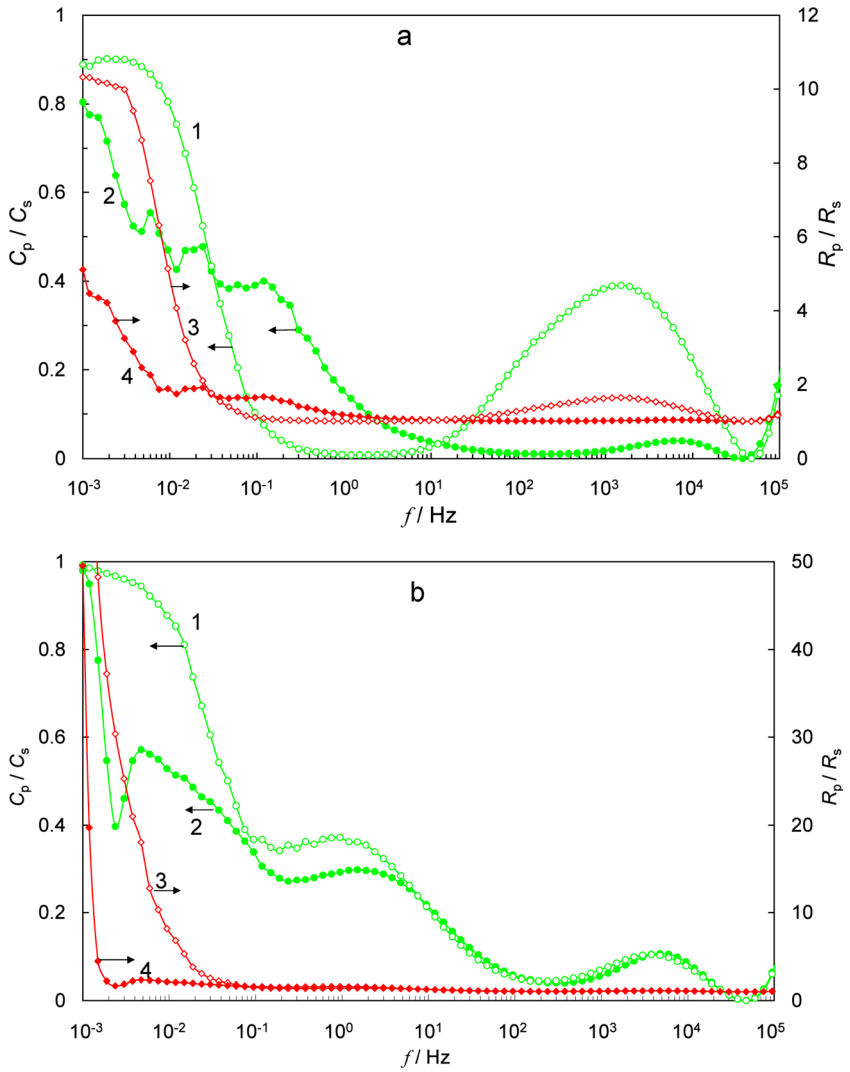

Fig. 11 Ratio of C_p/C_s (*1*, *2*) and R_p/R_s (*3*, *4*) for 1 M Na_2SO_4 (**a**) and 1 M Rb_2SO_4 (**b**) based SC at $\Delta E=1.0$ V (*open marks*) and $\Delta E=2.0$ V (*filled marks*)

mesoporous–macroporous regions of Mo_2C-CDC electrodes, respectively. Thus, a comparison of data with our previous work [23] and data in Fig. 9c shows that the ΔE has very noticeable influence on the medium- and low-frequency process parameters.

Based on the Orazem et al. model [42] within the high-frequency region, the slope of log $|-Z''|$, log f plot is nearly −0.85, indicating the mixed kinetics adsorption, mass transfer step and faradic processes at the Rb_2SO_4 | Mo_2C-CDC or Na_2SO_4 | Mo_2C-CDC interfaces. More detailed analysis of log $|-Z''|$, log f plots demonstrates that the slope value of log $|-Z''|$, log f plot for the Rb_2SO_4-based system is somewhat less negative (−0.92) compared with the Na_2SO_4-based system, indicating the more pronounced deviation of the Rb_2SO_4+ H_2O | Mo_2C-CDC supercapacitor system from the ideally polarisable electrode model. Within the medium-frequency region $1.0<f<100$ Hz, there are linear areas in log $|-Z''|$, log f plots with the slope nearly zero, indicating that within this frequency region, the slow faradic processes determine the kinetics behaviour of the SC under study.

The absolute values of the imaginary part of impedance strongly depend on ΔE applied and at fixed ΔE=2.0 V are lower for the Rb_2SO_4-based SC compared with the Na_2SO_4-based system. With the increase of ΔE from 1.0 to 2.0 V, $|-Z''|$ values increase, indicating that capacitance values increase with ΔE applied. At very low ac frequency and very high ΔE=2.0 V, the limiting rate-determining process is the very slow faradic charge transfer step (the slope of log $|-Z''|$, log f plots is nearly zero for both systems under study [42–44], but at ΔE=1.0 V, nearly ideal capacitive behaviour has been established (slope −0.95) [23].

The values of gravimetric series (C_s) and parallel (C_p) capacitances (Figs. 10a, b), calculated from the Nyquist plots ($Z''=-1/(j2\pi fC_s$; $C_p=C_s/(1+\tan^2\delta)$; $\tan\delta=Z'/Z''$), are in a good agreement with the values of $C_{m;CV}$ and C_{CC} only at very low ac frequency ($f\leq 1$ mHz). C_s weakly increases in the order 1 M $Na_2SO_4\leq$1 M Rb_2SO_4 aqueous electrolyte-based supercapacitors. At higher frequency, there is a well-expressed dependence of C_s or C_p on f for the all electrolyte systems studied, caused by the faradic reactions as well as by the small ac penetration depth compared with the pore length.

It should be mentioned that the essential increase of the *IR*-drop inside of the microporous carbide-derived carbon electrode matrix, expressed as R_s and R_p ($R_s=Z'$) and $R_p=R_s(1+1/\tan^2\delta)$, with the increase of cycle number analysed, explained by the accumulation of gaseous products and electrodeposited non-conducting intermediates onto/into the electrode surface, has been observed for both electrolytes. However, the less-pronounced dependence of C_s and R_s on f (as well as C_p and R_p) and $C_p/C_s\approx 1.0$ at $f\rightarrow 0$ Hz for 1 M Rb_2SO_4 at ΔE=1.0 V (Fig. 11a, b) indicates that for this electrolyte, the distances of the maximal approach of cations onto the Mo_2C-CDC porous system are shorter and the quicker establishment of the adsorption equilibrium has been established at relatively moderate ac frequency (f_{low}=10 mHz). At $f\leq 1$ mHz, the ratio of C_p/C_s is very close to unity which indicates that the blocking adsorption step-limited processes at Mo_2C-CDC | 1 M Na_2SO_4 or 1 M Rb_2SO_4+H_2O interface are taking place at ΔE=1.0 V. At ΔE=2.0 V and $f\leq 1$ mHz, C_p/C_s for the Na_2SO_4-based system is nearly 0.8 and, for Rb_2SO_4, lower R_p/R_s values at ΔE=2.0 V differently from ΔE=1.0 V have been calculated at $f\rightarrow 0$, indicating that adsorption-limited faradic reduction processes are prevailing at the Rb_2SO_4-based supercapacitor. At $f\rightarrow 0$, for the Rb_2SO_4-based system, somewhat higher increase of R_p/R_s has been observed explained by more effective surface blocking compared with the Na_2SO_4-based SC. However, more detailed time stability tests are inevitable for SC applications under development.

Conclusions

The analysis of impedance data demonstrates very complex kinetics behaviour of completed devices (adsorption and blocking adsorption, faradic, mass transfer, reduction of Na^+ and Rb^+ ions and intercalation, surface oxidation, gas adsorption, ionisation, etc.) at $\Delta E\geq 1.5$ V. At least four different characteristic time constants dependent on the electrolyte cation composition and cell potential applied have been calculated and discussed. Preliminary non-linear least squared fitting data show that low and high Rb_2SO_4-based system frequency inductive effect (characteristic of the decomposition of cell components) must be taken into account to have a reasonable fitting of calculated Nyquist plots with experimental data.

Acknowledgments This work was supported by the Estonian Science Foundation under Project No. 9184, Estonian Ministry of Education and Research project SF0180002s08, European Regional Development Fund Project SLOKT10209T, Estonian Centre of Excellence in Research Project TK117T "High-technology Materials for Sustainable Development" and Project IUT20-13.

References

1. Conway BE (1999) Electrochemical supercapacitors: scientific fundamentals and technological applications. Kluwer Academic/Plenum Publishers, New York
2. Burke A (2000) J Power Sources 91:37–50
3. Kötz R, Carlen M (2000) Electrochim Acta 45:2483–2498
4. Chmiola J, Yushin G, Gogotsi Y, Portet C, Simon P, Taberna PL (2006) Science 313:1760–1763
5. Miller JR, Simon P (2008) Science 321:651–654
6. Simon P, Gogotsi Y (2008) Nat Mater 7:845–854
7. Salitra G, Soffer A, Eliad L, Cohen Y, Aurbach D (2000) J Electrochem Soc 147:2486–2493
8. Jänes A, Permann L, Arulepp M, Lust E (2004) Electrochem Commun 6:313–318

9. Jänes A, Kurig H, Lust E (2007) Carbon 45:1226–1233
10. Jänes A, Thomberg T, Lust E (2007) Carbon 45:2717–2722
11. Jänes A, Thomberg T, Kurig H, Lust E (2009) Carbon 47:23–29
12. Eliad, Salitra G, Soffer A, Aurbach D (2005) Langmuir 21:3198–3202
13. Wang Y, Chen KS, Mishler J, Cho SC, Adroher XC (2011) Appl Energy 88:981–1007
14. Carmo M, Fritz DL, Mergel J, Stolten D (2013) Int J Hydrogen Energy 38:4901–4934
15. Härk E, Nerut J, Vaarmets K, Tallo I, Kurig H, Eskusson J, Kontturi K, Lust E (2013) J Electroanal Chem 689:176–184
16. Lee HY, Goodenough JB (1999) J Solid State Chem 144:220–223
17. Portet C, Lillo-Ródenas MÁ, Linares-Solano A, Gogotsi Y (2009) Phys Chem Chem Phys 11:4943–4945
18. Roldan S, Villar I, Ruiz V, Blanco C, Granda M, Menendez R, Santamaria R (2010) Energy Fuels 24:3422–3428
19. Jänes A, Lust E (2006) J Electroanal Chem 588:285–295
20. Jänes A, Lust E (2006) J Electrochem Soc 153:A113–A116
21. Thomberg T, Jänes A, Lust E (2009) J Electroanal Chem 630:55–62
22. Lota G, Frackowiak E (2009) Electrochem Commun 11:87–90
23. Eskusson J, Jänes A, Kikas A, Matisen L, Lust E (2011) J Power Sources 196:4109–4116
24. Khomenko V, Raymundo-Piñero E, Béguin F (2010) J Power Sources 195:4234–4241
25. Bichat MP, Raymundo-Piñero E, Béguin F (2010) Carbon 48:4351–4361
26. Demarconnay L, Raymundo-Piñero E, Béguin F (2010) Electrochem Commun 12:1275–1278
27. Gao Q, Demarconnay L, Raymundo-Piñero E, Béguin F (2012) Energy Environ Sci 5:9611–9617
28. Damaskin BB, Petrii OA, Tsirlina G (2006) Electrochemistry. Khimia, Moscow
29. Frumkin AN (1987) Elektrodnye protsessy (The electrode processes). Nauka, Moscow
30. Conway BE (1965) Theory and principles of electrode processes. Ronald, New York
31. Trasatti S, Lust E, in White RE, Bockris J O'M, Conway BE (eds) (1999) Modern aspects of electrochemistry. vol 33 Kluwer Academic/Plenum Publishers, New York, p 1
32. Lust E, in: Bard JA, Stratman M (eds) (2002) Encyclopedia of electrochemistry, Wiley–VCH, Weinheim, pp 188–224
33. Frumkin AN, in: Yeager E (ed) (1961) Advances in electrochemistry and electrochemical engineering. New York, Wiley, pp 1-15
34. Frumkin AN (1965) J Electroanal Chem 9:173–183
35. Bian X, Scanlon MD, Wang S, Liao L, Tang Y, Liu B, Girault HH (2013) Chem Sci 4:1432–1441
36. Chizmadzhev YA, Chirkov YG, in: (Yaeger E, Bockris JOM, Conway BE . Sarangapani S (eds) (1983) Comprehensive treatise of electrochemistry. Plenum Press, New York, pp 317-91
37. Tõnisoo A, Kruusma J, Pärna R, Kikas A, Hirsimäki M, Nõmmiste E, Lust E (2013) J Electrochem Soc 160:A1084–A1093
38. Lust E, Jänes A, Sammelselg V, Miidla P (2000) Electrochim Acta 46:185–191
39. Lust E, Jänes A, Arulepp M (2004) J Solid State Electrochem 8:488–496
40. Jänes A, Permann L, Arulepp M, Lust E (2004) J Electroanal Chem 569:257–269
41. Nurk G, Jänes A, Lust K, Lust E (2001) J Electroanal Chem 515:17–32
42. Orazem ME, Pébère N, Tribollet B (2006) J Electrochem Soc 153: B129–B136
43. Lasia A (2006) J Electroanal Chem 593:159–166
44. Macdonald JR, Johnson WB (1987) Fundamentals of impedance spectroscopy. In: Macdonald JR (ed) Impedance spectroscopy. Wiley, New York, pp 1–26